Interplay between tightly focused excitation and ballistic propagation of polariton condensates in a ZnO microcavity

R. Hahe,[1] C. Brimont,[1] P. Valvin,[1] T. Guillet,[1,*] F. Li,[2,3] M. Leroux,[2] J. Zuniga-Perez,[2] X. Lafosse,[4] G. Patriarche,[4] and S. Bouchoule[4]

[1]*Laboratoire Charles Coulomb (L2C), UMR 5221, Centre national de la recherche scientifique (CNRS)-Université de Montpellier, Montpellier, France*

[2]*Centre de Recherche sur l'Hétéro-Epitaxie et ses Applications (CRHEA)-CNRS, Rue Bernard Gregory, 06560 Valbonne, France*

[3]*Université de Nice Sophia-Antipolis, 06103 Nice, France*

[4]*Laboratoire Photonique et Nanostructures (LPN)-CNRS, Route de Nozay, 91460 Marcoussis, France*

(Received 22 October 2015; revised manuscript received 30 November 2015; published 23 December 2015; corrected 20 January 2016)

The formation and propagation of a polariton condensate under tightly focused excitation is investigated in a ZnO microcavity both experimentally and theoretically. Two-dimensional (2D) near-field and far-field images of the condensate are measured under quasicontinuous nonresonant excitation. The corresponding spatial profiles are compared to a model based on the Gross-Pitaevskii equation under cylindrical geometry. This paper allows one to connect the experiments performed with a small excitation laser spot and the previous kinetic models of condensation in a 2D infinite microcavity and to determine the relevant parameters of both the interaction and the relaxation between the reservoir and the condensate. Two main parameters are identified: The exciton-photon detuning through the polariton effective mass and the temperature, which determines the efficiency of the relaxation from the reservoir to the condensate.

DOI: 10.1103/PhysRevB.92.235308 PACS number(s): 42.65.Sf, 71.36.+c

I. INTRODUCTION

Polaritons are able to propagate over tens to hundreds of microns [1]. The analogy between the polaritons' trajectory under a constant cavity gradient and the free fall evidenced the ballistic character of this propagation [2,3]. The momentum of a polariton condensate can also be controlled either by resonant excitation (through the wave vector of the exciting laser) or under nonresonant excitation (through the spatial shape of the exciton reservoir). This last feature has been demonstrated in the case of one-dimensional (1D) polariton condensates, showing the intricate roles of propagation and reservoir repulsion in the generation and amplification of the polariton condensate [4]. This has motivated many demonstrations of polariton devices based on condensates put into motion in an analog way to electrons in microelectronic devices; those include polariton transistors [5] and polariton tunneling diodes [6] and proposals of optical amplifiers [7]. The propagating character of polaritons is also underlying striking features of the condensates (e.g. vortices [8,9], solitons [10–13]), so that they are now considered as "quantum fluids" governed by nonlinear hydrodynamics [14].

Most of the recent demonstrations of polariton lasing in ZnO, GaN, and organic microcavities have been performed under the so-called "tightly focused excitation regime," where the excitation laser needs to be focused over a spot only a few microns in diameter in order to reach the threshold for polariton lasing [15–24]. This is due both to the high excitation density required for condensation and, most importantly, to the presence of photonic disorder or inhomogeneities in the cavity. As discussed by Wouters and Carusotto [25] and Wouters *et al.* [26], this implies that the propagation of the polariton condensate plays an important role in its formation, even though the emission is usually spatially integrated during the spectroscopy experiments.

The aim of this paper is to provide insight into the interplay between the tightly focused excitation commonly employed by the room-temperature polaritonics community and the formation and propagation of the polariton condensate and of its excitonic reservoir. This interplay will be illustrated by monitoring the spatial distribution of both the polariton condensate and the reservoir below and above threshold. The condensate distribution will then be compared to a model describing the ballistic propagation of the condensate under the repulsion of the reservoir in a cylindrical geometry and neglecting polariton relaxation. This allows evaluating whether the condensation threshold only depends on the local density of the exciton reservoir or if it is influenced by the outwards flux of polaritons. In this last regime, the condensation threshold density is increased compared to the case of an infinite two-dimensional (2D) condensate, and this increase will be estimated. Boundary values of the corresponding physical parameters can be then extracted. The study is performed on a high Q planar microcavity with low photonic disorder [20,27] but displaying regions with either a steep photonic potential (induced by a relatively large cavity thickness gradient) or with an almost flat photonic landscape. The interplay between condensation and propagation is investigated as a function of the detuning of the polariton mode, of the temperature (at 80 and 300 K), as well as of the presence or absence of a thickness gradient in the cavity.

II. THE SAMPLE AND ITS LOCAL PHOTONIC LANDSCAPE

The investigated sample is a ZnO-bulk microcavity displaying polariton lasing over a wide range of exciton-photon detunings and temperatures. Earlier works described its fabrication [27] and the measured and modeled phase diagram

*Thierry.Guillet@umontpellier.fr

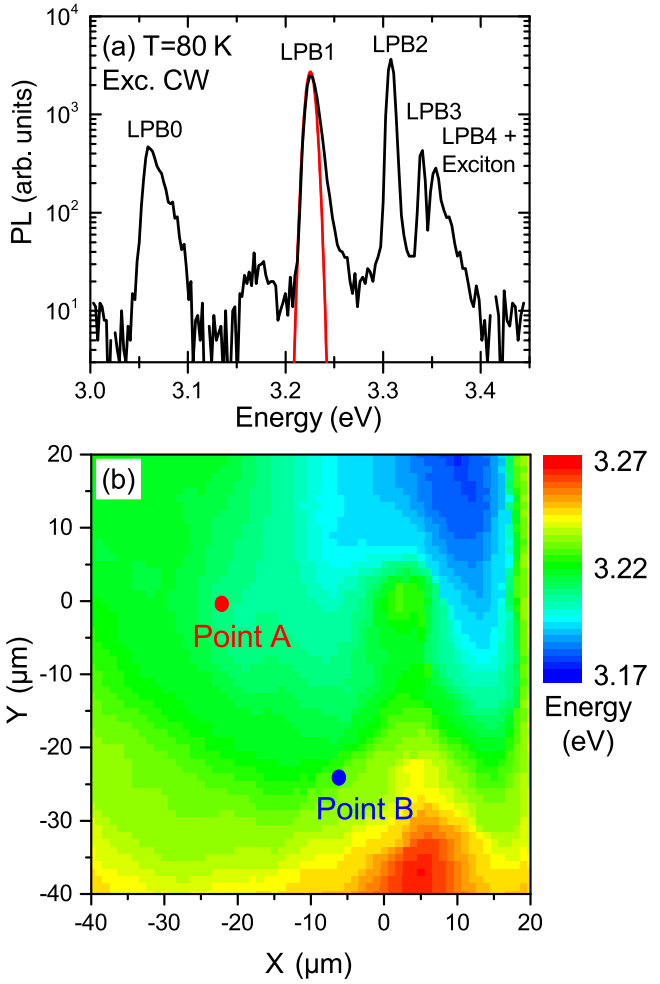

FIG. 1. (Color online) (a) Confocal μPL spectrum of the microcavity at $T = 80$ K, under CW excitation; the low energy part of the LPB1 line is fitted with a Gaussian line shape (red line). (b) Energy map of the LPB1 line measured under scanning confocal μPL (deduced from the Gaussian fit) at 80 K. The spectrum (a) is measured at the position $(-6\,\mu\text{m}, -26\,\mu\text{m})$. The two points of interest investigated in Sec. III are labeled A and B.

of polariton condensation [20]. The tunability of this polariton laser results from the high crystalline quality of the ZnO active layer, the large quality factor (up to 4000) and the wide stopbands provided by the dielectric SiO_2/HfO_2 Bragg reflectors.

Work for this paper has been performed on an area where the excitons are coupled to the 4λ and 4.5λ cavity modes (comparable to Fig. 4 in Ref. [20]). This large cavity thickness assures efficient heat dissipation and prevents any undesirable heating even at high pumping intensities. Prior to the investigation of polariton propagation, it is necessary to measure the photonic landscape that is felt by polaritons. The photoluminescence spectrum [Fig. 1(a)] consists of multiple transitions related to each of the polariton branches (each one of them associated to the coupling of excitons to distinct cavity modes) and the bare excitons. In order to enhance the spatial resolution of the photonic potential map, confocal microscopy has been used instead of microphotoluminescence (μPL) experiments spatially integrating all the emission. In a confocal μPL configuration, the sample is excited with a nonresonant continuous-wave laser ($\lambda = 266$ nm) far from the condensation threshold (thereby preventing any density-dependent blueshift). The excitation spot has a diameter of the order of 1 μm; it is scanned over $60 \times 60\,\mu\text{m}^2$ with 1 μm steps. The spatial filtering is provided horizontally by the entrance slit of the spectrometer and vertically by selecting a single row of the charge-coupled device (CCD) detector at the output of the imaging spectrometer. The confocal resolution is $0.7 \times 1.5\,\mu\text{m}^2$ (as measured in Ref. [28]). The confocal microscopy allows one to enhance the spatial resolution of such a map, compared to a μPL experiment spatially integrating all the emission. Figure 1(b) presents a mapping of the polariton mode (LPB1), arising from the coupling of ZnO excitons with the 4.5λ cavity mode. The precise modeling of the polariton dispersions is discussed in detail in Appendix A. The coupling parameters are presented in Table I. At the point A, the detuning of the LPB1 branch is equal to 5 ± 10 meV. The corresponding Rabi splitting is around 280 ± 30 meV.

The investigated area presents various cavity thickness gradients depending on the exact location. For example, a small gradient (< 0.3 meV μm^{-1}) is measured for the branch LPB2 at the point named A, whereas a much stronger gradient (0.8 meV μm^{-1} for LPB2) is found at point B. Those two points have been chosen for the detailed propagation imaging performed in the next section. The corresponding energy gradients for the polariton branch arising from the 4.5λ cavity mode (LPB1), which displays a larger photonic fraction, are 0.5 and 1.5 meV μm^{-1}, respectively. We should notice that the energies of the polariton branches at both positions only differ by 10 meV, i.e. less than 5% of the Rabi splitting, so that their exciton-photon compositions are very similar.

III. 2D IMAGING OF THE EXCITON RESERVOIR AND THE POLARITON CONDENSATE

The investigation of the spatial dynamics of the polariton condensate across its generation threshold requires a complete imaging of the exciting laser, the initially generated reservoir, and the polariton emission from each emitting branch, below and above the condensation threshold. We here name "reservoir" the ensemble of all particles (excitons, polaritons with large wave vectors) able to relax towards the condensate and emitting at energies close to the bare exciton energy. Work for this paper was performed through 2D tomography. Contrary to the confocal imaging setup described in the previous section, the sample is now excited with a fixed laser spot; its emission is collected by the microscope objective and imaged by an ultraviolet (UV) achromatic lens on the entrance plane of the imaging spectrometer. The entrance slit filters the signal originating from a slice of the emission that is then spectrally dispersed by the grating and recorded by the CCD detector. The motorized translation of the last lens in the direction perpendicular to the slit allows reconstructing the full 2D image of the emission with spectral resolution. As in part of our previous works [15,20], the polariton condensate is generated under quasi-continuous-wave (cw) optical pumping with a Q-switched laser providing 400 ps pulses at 266 nm (repetition rate: 4 kHz) since polariton condensation cannot be reached under cw excitation at this wavelength.

TABLE I. Main polariton parameters relevant for the experiments and simulations presented in the Secs. III and IV, as obtained from the transfer-matrix simulations at normal incidence, the coupled oscillator model, and the experiments. The cavity thickness is $L = 890$ nm.

			$T = 300$ K			$T = 80$ K		
			LPB0	LPB1	LPB2	LPB0	LPB1	LPB2
	Exciton X_A	Energy (eV)		3.300			3.368	
Transfer-matrix	Bare cavity modes	Energy (eV)	3.047	3.305	3.568	3.047	3.305	3.568
		Effective mass	3.7E − 5	4.7E − 5	5.0E − 5	3.7E − 5	4.7E − 5	5.0E − 5
		Detuning (meV)	−253	5	268	−321	−63	200
	Polariton branches	Energy (eV)	3.005	3.181	3.256	3.012	3.210	3.315
		Effective mass	3.9E − 5	7.5E − 5	2.9E − 4	4.1E − 5	8.7E − 5	3.5E − 4
		$x = \frac{\partial E_{\mathrm{LPB}}}{\partial E_X}$	0.12	0.48	0.87	0.09	0.36	0.81
		$\frac{\partial E_{\mathrm{LPB}}}{\partial L}$ (meV nm^{-1})	−1.7	−1.3	−0.34	−1.8	−1.7	−0.5
Coupled oscillators	Polariton branches	Energy (eV)	3.005	3.181	N/A	3.012	3.210	N/A
		Effective mass	4.5E − 5	6.5E − 5	N/A	4.5E − 5	6.5E − 5	N/A
		Rabi energy (meV)	280 ± 30		N/A	280 ± 30		N/A
		$\lvert c_X \rvert^2$	0.15	0.32	N/A	0.10	0.27	N/A
Experiment (Pt. A)	Polariton branches	Energy (eV)	3.035	3.187		3.056	3.222	3.310
		Effective mass	3.5E − 5	7.1E − 5				
		Condensation		X				X

A. Imaging the polariton condensation in a branch at zero detuning

Let us first investigate the condensation process at a temperature of 300 K. The power-dependent series of spectra across polariton condensation are presented in Fig. 2. The spectra consist of two transitions attributed to each polariton branch. Condensation is observed on the polariton branch close to zero detuning (LPB1). A blueshift of about 4 meV is measured at threshold, reflecting the repulsive potential induced by the generated excitons and felt by the polaritons. The spectra are measured with a low resolution in order to observe all transitions in a single acquisition.

The integrals of each of the transitions, as well as the weak signal corresponding to the scattered excitation laser,

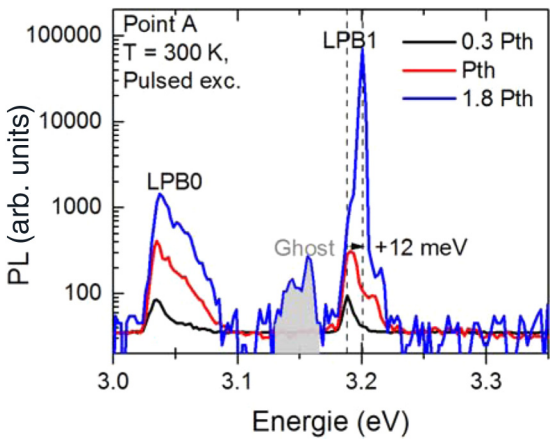

FIG. 2. (Color online) μPL spectra at point A as a function of the excitation power, under pulsed excitation at $T = 300$ K. The threshold for polariton condensation is $P_{\mathrm{th}} = 0.94$ nJ/pulse. The ghost of the spectrometer is related to the very intense peak of the polariton condensate and indicated by a gray shade.

are then calculated at each of the points in the 2D emission plane (near field image). An additional lens allows projecting the back focal plane of the microscope objective onto the entrance plane of the spectrometer; the 2D Fourier plane of the emission is therefore measured under the exact same excitation conditions (far field image). The corresponding images ($P = 1.7\ P_{\mathrm{th}}$, $T = 300$ K) are presented in Fig. 3 (near field) and Fig. 4 (far field), as measured at the two points named A and B in Fig. 1. The main information deduced from the spectra and the tomographies is presented in the Table II. The features are very similar at both points:

(i) Laser spot [Figs. 3(a) and 3(b)]: It extends over 4 μm full width at half maximum (FWHM), and it can be fitted by a Gaussian. However, it presents tails in some specific directions, which are identical at both points. They are attributed to the multimode character of the Q-switched laser source. The available laser power being close to the polariton laser threshold, it is unfortunately not possible to perform any spatial filtering of the laser modes in order to suppress these tails before exciting the sample.

(ii) Uncondensed LPB0 and LPB1 branches: The spatial distribution of the uncondensed LPB0 branch [Figs. 3(c) and 3(d)], as well as the one of the LPB1 branch below threshold (not shown) are slightly broader than the laser spot (5–6 μm FWHM). The distribution of LPB0 is centered at the laser spot in the case of point A (almost flat photonic landscape), whereas it shifts by about 3 μm in the case of point B (in the presence of a thickness gradient). The corresponding 2D far-field patterns are described in Appendix B. They present a cylindrical symmetry at point A that is broken due to the photonic gradient at point B. This reflects the impact of the photonic gradient on the polariton relaxation in a mostly photonic branch, leading to a nonzero average velocity of LPB0 polaritons. Even if the propagation properties of uncondensed polaritons are beyond the scope of this paper, those features are a clear signature of the presence of a thickness gradient.

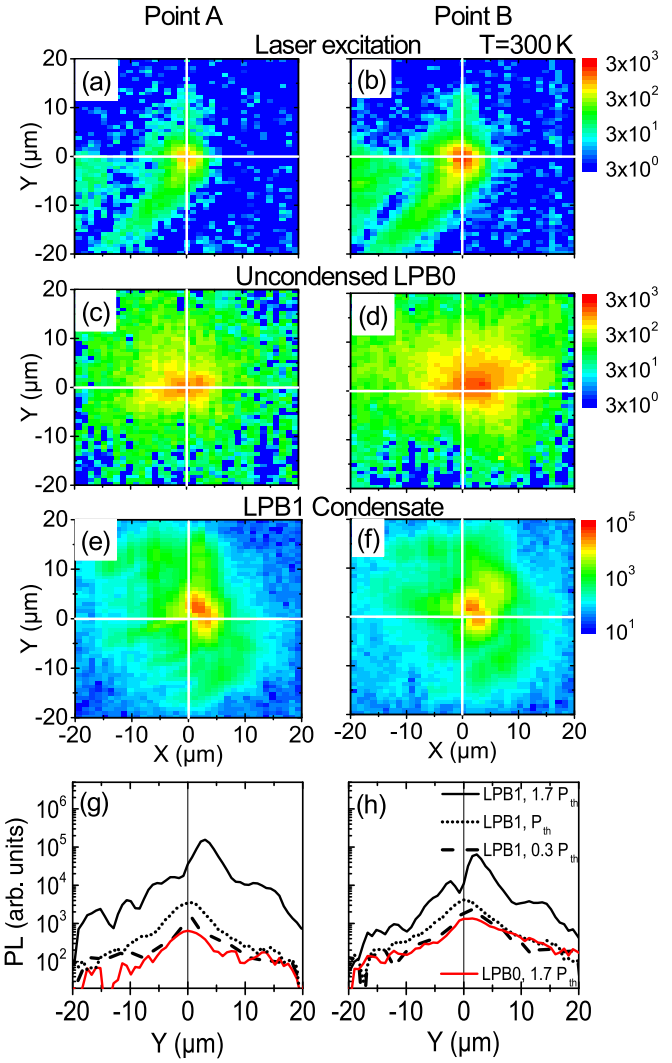

FIG. 3. (Color online) Near-field images under pulsed excitation at $P = 1.7\ P_{\rm th}$, $T = 300$ K. The points A [(a), (c), (e), and (g), flat landscape] and B [(b), (d), (f), and (h), slope along Y] correspond to the positions indicated in Fig. 1. The signal is integrated at the energy of (a) and (b) the exciting laser, (c) and (d) the LPB0 line, and (e) and (f) the LPB1 line. (g) and (h) Cross-sections are extracted along the Y direction. The FWHM of the corresponding profiles at $P_{\rm th}$ are given in Table II.

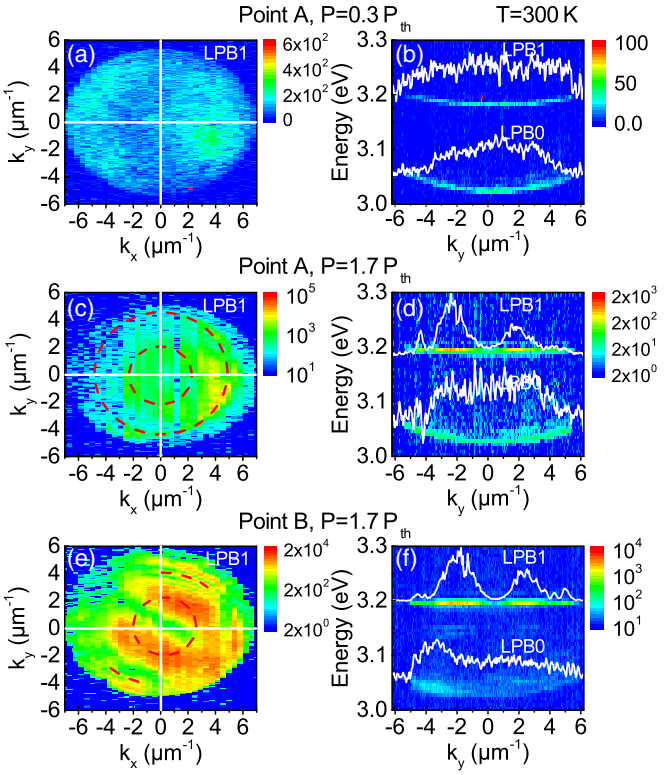

FIG. 4. (Color online) Far-field images of the LPB1 line under pulsed excitation at point A (a) below and (c) above threshold, and (e) point B above threshold, $T = 300$ K. The red dashed circles are guides for the eye. (b), (d), and (f) The corresponding spectrally resolved vertical cross-sections extracted at $k_x = 0$. (a) and (b) Linear false color scales are used below threshold and (c)–(f) logarithmic ones above threshold.

(iii) Condensed LPB1 branch: The spatial distribution of the polariton condensate [LPB1, Figs. 3(e) and 3(f)] presents structured patterns; contrary to the images of the exciton reservoir and the uncondensed polaritons, it is not monotonically decreasing with the distance to the center of the laser spot, and it presents sharp angular patterns. The images are very similar at both points A and B. The far field images of the condensate (Fig. 4), recorded at the same points, are characterized by a minimum of the signal at $k = 0$, a first broad emission ring at $k \approx 2\ \mu{\rm m}^{-1}$, and additional rings or portions of rings at a larger wave vector, as indicated by the red dotted circles. They may extend beyond the accessible angular range of our present microscope objective (numerical aperture [NA] 0.4, i.e. $k < 6\ \mu{\rm m}^{-1}$). The vanishing signal at zero wave vector and the well-defined wave vector of the condensates [see Figs. 4(d) and 4(f)] are characteristic of a ballistic ejection of the condensate generated at the excitation spot and repelled by the generated excitons [4,16,29]. This will be modeled in detail in Sec. IV. The absence of a proper

TABLE II. Parameters of the imaging experiments under tightly-focused excitation (from Figs. 2, 3, and 5).

	$T = 300$ K				$T = 80$ K				
	Laser	Reservoir	LPB0	LPB1	Laser	Reservoir	LPB0	LPB1	LPB2
Condensate				X					X
Spatial FWHM	$4\ \mu$m		$5\ \mu$m	$6\ \mu$m	$4\ \mu$m	$4.5\ \mu$m	$4\ \mu$m	$4\ \mu$m	$2\ \mu$m
Blueshift at threshold	$P_{\rm th} = 0.94$ nJ per pulse		3 meV	4 meV	$P_{\rm th} = 0.36$ nJ per pulse		2 meV	3 meV	8 meV
Blueshift beyond threshold	$P = 1.7 P_{\rm th}$		5 meV	12 meV	$P = 1.3 P_{\rm th}$		3 meV	5 meV	11 meV

cylindrical symmetry of the near-field and far-field images and the similarities observed at both sample positions lead us to conclude that the precise shape of the condensate is mostly governed by the shape of the excitation laser and its distortion compared to a purely monomode Gaussian spot. This proves that, under the current experimental conditions, the shape of the condensate is not reflecting the local potential felt by polaritons, induced by photonic or excitonic disorder or gradients in the investigated cavity. This is a first indication of a strong difference with the condensation in the ZnO cavity investigated in Ref. [30], where the disorder plays a major role in the patterning of the condensate. This allows us to compare the measured condensate profiles to a model that does not take photonic gradients into account and that does not include disorder. Let us finally emphasize that the complexity of the condensate spatial patterning is underestimated when only cross-sections of the far-field image are recorded [Figs. 4(d) and 4(f)].

B. Imaging the polariton condensation in a branch at positive detuning

The same study has been performed at $T = 80\,\mathrm{K}$ (Fig. 5 and Table II). The three main differences with the room-temperature case are the following:

(i) The relaxation of excitons towards the various polariton branches favors the most excitonic polaritons, so that condensation is first observed on the LPB2 branch (detuning $+200 \pm 40$ meV). This is consistent with the systematic study presented in Ref. [20]: The phonon-assisted relaxation is less efficient for this temperature, so that the relaxation kinetics are mainly governed by exciton-exciton scattering, and therefore, condensation is now observed in LPB2, whose excitonic fraction is larger than that of LPB1.

(ii) A transition close to the energy of the uncoupled excitons is now observed at 3.34–3.37 eV; it is attributed to higher order polariton modes, which are almost purely excitonlike [14,20], and the emission of uncoupled excitons. The 2D spatial image of this last transition provides direct access to the spatial distribution of the reservoir, which is fitted by a Gaussian profile. The diameter of the reservoir ($4.5\,\mu$m FWHM) is comparable to the one of the laser spot ($4\,\mu$m FWHM). The LPB1 branch (now at a slightly negative detuning of -60 meV due to the temperature variation of the exciton energy) presents a distribution very similar to the one of the exciton reservoir [Fig. 5(b)].

(iii) The profile of the LPB2 emission differs from the one of the exciton reservoir and the LPB1 branch since it is much sharper near $r = 0\,\mu$m [Fig. 5(b)], leading to a FWHM twice as small than the one of the exciton reservoir. The relative intensity of this sharp component compared to the long tails increases when the excitation power is increased beyond threshold. The situation is therefore different from the case of a condensate at zero detuning investigated in Sec. III A, where the increase of the condensate particle number led to an outward propagation of the condensate and a profile with a maximum at $r = 2\,\mu$m.

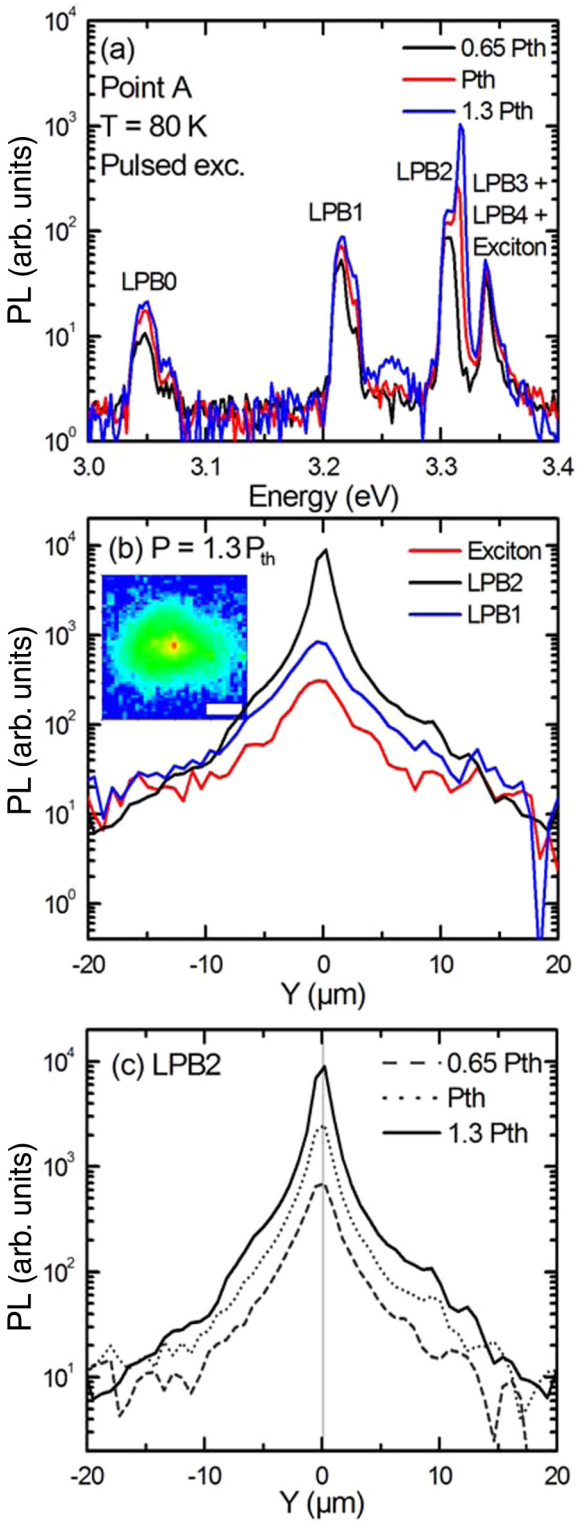

FIG. 5. (Color online) (a) μPL spectra at point A as a function of the excitation power, under pulsed excitation at $T = 80\,\mathrm{K}$. (b) Cross-sections of the exciton reservoir, the uncondensed LPB1 branch, and the polariton condensate (LPB2) at $P = 1.3\ P_{\mathrm{th}}$. The inset presents the 2D image ($10\,\mu$m scale bar) of the polariton condensate in false colors (logarithmic scale from blue to red). (c) Cross-section of the LPB2 emission as a function of the excitation power. The FWHM of the corresponding profiles at P_{th} are given in Table II.

IV. MODEL

A. Generation and propagation of the polariton condensate in a cylindrical geometry

The role of propagation in the polariton condensation was theoretically explored in the work of Wouters and Carusotto [25] and Wouters *et al.* [26]. They defined, in particular, the tightly focused excitation regime that corresponds to our present experimental conditions, as well as that employed in many other papers on polariton condensates. Here, we follow this model, assuming a cylindrical symmetry and neglecting the energy relaxation of the polaritons. This model is well adapted to polariton condensates that propagate in a ballistic way, i.e. with a well-defined wave vector at a given position, as we observed in Figs. 4(d) and 4(f). The specificity of this paper lies in the ability to determine most of the parameters in the case of bulk-ZnO polariton condensates, or provide bounds to them, from the comparison with a detailed set of experiments.

The model describes the kinetics of the exciton reservoir and a single polariton condensate. The density n_R of the reservoir is described by a rate equation

$$\frac{dn_R(\boldsymbol{r})}{dt} = P(\boldsymbol{r}) - \gamma_R\, n_R(\boldsymbol{r}) - R\, n_R(\boldsymbol{r})\, |\psi(\boldsymbol{r},t)|^2. \quad (1)$$

The condensate wave function $\psi(\boldsymbol{r})$ is obtained in a mean-field approximation as the solution of the Gross-Pitaevskii equation (GPE) in the absence of any external potential:

$$i\hbar\frac{\partial\psi(\boldsymbol{r},t)}{\partial t} = \left(\hbar\omega_0 - \frac{\hbar^2}{2\,m^*}\nabla_r^2 + \frac{i\hbar}{2}(R\, n_R(\boldsymbol{r}) - \gamma_{\rm pol}) + \hbar g_R\, n_R(\boldsymbol{r}) + \hbar g\, |\psi(\boldsymbol{r},t)|^2\right)\psi(\boldsymbol{r},t), \quad (2)$$

where $\hbar\omega_0$, m^*, and $\gamma_{\rm pol}$ are respectively the energy, the effective mass, and the decay rate of the investigated polariton branch; g_R and g are the exciton-polariton and polariton-polariton interaction constants, respectively. The stimulated relaxation from the reservoir to the condensate is accounted for through the term $R\, n_R(\boldsymbol{r})$, depending linearly on the reservoir density. The reservoir consists both of excitons, with wave vectors beyond the light cone in the ZnO active layer, and high-energy polaritons beyond the so-called bottleneck region; its decay rate is denoted γ_R. A Gaussian profile is chosen for the pumping rate in the reservoir $P(r)$ according to the measured exciton reservoir (4.5 μm FWHM). We neglect here the terms corresponding to the disorder and/or the photonic gradient in the microcavity, as discussed at the end of the Sec. III A.

Following the approach developed for small excitation spots under stationary excitation and cylindrical symmetry in Ref. [26], the condensate wave function at a given blueshift ($\hbar\omega_c - \hbar\omega_0$) writes $\psi(r,\theta,t) = \psi_m(r)e^{-i\omega_c t}e^{im\theta}$. In this paper, we only consider the vortex-free case of $m = 0$ (no angular momentum in the condensate). For radii r much larger than the spot size, the stationary solution freely propagates with a wave vector $k_c = \sqrt{2m^*/\hbar(\omega_c - \omega_0)}$ and vanishes due to the finite polariton lifetime, so that it asymptotically follows the Hankel function $H_0^{(1)}(\sqrt{2m^*/\hbar\,(\omega_c - \omega_0 + i\gamma_{\rm pol}/2)}\cdot r)$. For $m = 0$ (no vortex) and an experimentally determined blueshift $\hbar(\omega_c - \omega_0)$, the full condensate wave function $\psi_0(r)$ is numerically calculated with a fourth-order Runge-Kutta algorithm.

The numerical resolution of the problem is then performed both in the case of a nondepleted reservoir ($n_R(r) = P(r)/\gamma_R$) and in the case of a depleted reservoir ($n_R(r) = P(r)/(\gamma_R + R|\,\psi_0(r)|^2)$), as deduced from Eq. (1). The two assumptions will be compared in Sec. V in order to conclude about the role of depletion in the condensation dynamics.

B. A procedure for the choice of the model parameters

The determination of the parameters of the GPE has a strong influence on the obtained solution. Some parameters have been directly extracted from measurements: Time-resolved photoluminescence experiments give access to the exciton reservoir lifetime $\tau_R = 40$ ps, leading to a reservoir recombination rate $\gamma_R = 0.016$ meV. The cavity decay rate $\gamma_{\rm cav} = 0.8$ meV is deduced from the measured quality factor $Q = 4000$ [27]. Each polariton branch is characterized by an effective mass that is measured in far-field dispersion for LPB0 and LPB1 (at $T = 300$ K), and deduced from transfer-matrix simulations for the heaviest branch LPB2 (observed only at $T = 80$ K). The full set of parameters for the polariton branches is presented in Table III.

Three parameters (g_R, g, and R) are unknown from experiments. The polariton interaction constants g_R and g are assumed to depend on the Hopfield coefficient of the investigated LPB, and the exciton-exciton interaction constant g_{XX}. As discussed in Appendix A, we prefer here to introduce the coefficient $x = \frac{\partial E_{\rm LPB}}{\partial E_X}$ instead of the Hopfield coefficient, so that the polariton-reservoir and polariton-polariton interaction constants read $g_R = x\cdot g_{XX}$ and $g = x^2\cdot g_{XX}$. The parameters g_R and g have been strongly debated in the study of GaAs microcavity polaritons and are still unknown for ZnO microcavities. Theoretical predictions in the case of interacting three-dimensional (3D) excitons in a slab [31] (corresponding to our bulk-ZnO microcavity) lead to a value $\hbar g_{XX}^a \approx 10\;\; E_b\, a_B^3/L \approx 1.8\quad 10^{-6}$ meV μm^2, where $E_b = 60$ meV and $a_B = 1.4$ nm are the ZnO binding energy and Bohr radius; $L = 890$ nm is the thickness of the ZnO active layer at the investigated point as discussed in Sec. II.

A second line of reasoning can be followed in order to determine those parameters: The parameter g_R can be also accessed through the measured blueshift of the polariton line at threshold $\hbar(\omega_c - \omega_0) = \hbar g_R.\, n_{R\,\rm th}$. Even if there is no independent experimental determination of the exciton density at threshold $n_{R\,\rm th}$, it has been calculated within a rate equation model in the 2D case of an infinite spot size in the same microcavity [20,32]: $n_{R\,\rm th}^{\rm 2D} \approx 5\cdot 10^4 \mu{\rm m}^{-2}$ at room temperature, which can be imposed to this value in our simulations. Following this approach, a second value of the interaction parameter will be deduced from the simulations shown in this section: $\hbar g_{XX}^b \approx 1.0\quad 10^{-5}$ meV μm^2, which is of the order of six times larger than g_{XX}^a. This apparent discrepancy will be discussed in Sec. V.

The gain rate R is phenomenological; in the 2D case of an infinite spot size, it is related to the reservoir density at threshold and the polariton decay rate $\gamma_{\rm pol}$ through $R\, n_{R\,\rm th}^{\rm 2D} = \gamma_{\rm pol}$ since gain and losses exactly compensate at the laser threshold. Contrary to the polariton interaction parameters,

TABLE III. Parameters of the numerical resolution of the GPE, corresponding to the Figs. 6 to 8. The input parameters of the model are indicated in italic.

	$T = 300$ K		$T = 80$ K
	$P = P_{\rm th}$	$P = 1.7P_{\rm th}$	$P = 1.3P_{\rm th}$
Condensate polariton branch	LPB1	LPB1	LPB2
Blueshift (meV)	*4*	*12*	*11*
$x = \frac{\partial E_{\rm LPB}}{\partial E_X}$	*0.47*	*0.47*	*0.87*
Polariton decay rate $\hbar\gamma_{\rm pol}$ (meV)	0.35	1.8	0.35
One reservoir assumption			
Exciton-exciton interaction $\hbar g^b_{XX}$ (eV μm^2)		*1.0E − 8*	
Exciton-polariton interaction $\hbar g_R$ (eV μm^2)	5.0E − 9	5.0E − 9	9.0E − 9
Stimulated relaxation rate $\hbar R$ (eV μm^2)	3.3E − 9	3.3E − 9	4.9E − 10
Exciton reservoir density $n_R(r=0)(\mu\text{m}^{-2})$	8.0E + 5	2.4E + 6	1.2E + 6
Equivalent threshold for 2D condensation (μm^{-2})	*5.0E + 4*	*5.0E + 4*	5.2E + 4
Hankel wave vector (μm^{-1})	2.8	4.9	9.2
Two reservoirs' assumption			
Exciton-exciton interaction $\hbar g^a_{XX}$ (eV μm^2)		*1.80E − 9*	
Exciton-polariton interaction $\hbar g_R$ (eV μm^2)	8.6E − 10	8.6E − 10	1.6E − 9
e-h pair reservoir density $n_R(r=0)(\mu\text{m}^{-2})$	4.6E + 6	1.4E + 7	6.9E + 7
Equivalent threshold for 2D condensation (μm^{-2})	2.9E + 5	2.9E + 5	3.1E + 5

it should depend on the temperature and the detuning of the polariton branch since it reflects the efficiency of the stimulated relaxation from the exciton reservoir to the polariton condensate. Again, its determination relies on the knowledge of $n^{\rm 2D}_{R\ \rm th}$.

In order to easily compare with the results of the rate equation model presented in Ref. [20], we have chosen the set of parameters based on $n^{\rm 2D}_{R\ \rm th} \approx 5 \cdot 10^4 \mu\text{m}^{-2}$, i.e. $\hbar g^b_{XX} \approx 1.0\ \ 10^{-5}$ meV μm^2 and $\hbar R = 5.\ 10^{-6}$ meV μm^2 at $T = 300$ K. Since the density of the exciton reservoir only appears through the terms $R\ n_R$ and $g_R\ n_R$ in the master Eqs. (1) and (2), it should be noticed that, in the absence of any strong reservoir depletion or strong polariton-polariton interactions, as we will show, the model leads to identical results for the condensate if we use the other set of parameters $\hbar g^a_{XX} \approx 1.8\ \ 10^{-6}$ meV μm^2 and $\hbar R = 8.6\ 10^{-7}$ meV μm^2 and exciton densities six times larger in the reservoir (see Table III). This point will be further discussed in Sec. V.

C. Simulations of a polariton condensate at zero detuning

The simulations corresponding to the experimental results of Fig. 3 are presented in Fig. 6. The adjustment of the simulation parameters to the experiment is performed in three steps:

(i) The known blueshift (4 meV at $P_{\rm th}$, 12 meV at 1.7 $P_{\rm th}$) and the effective mass of the polariton branch LPB2 determine the value k_c of the polariton wave vector far from the reservoir.

(ii) The long-distance tails of the condensate profile are compared to the model, for radii larger than the reservoir FWHM. The slope of the profile tails requires a slight adjustment of the polariton decay rate $\gamma_{\rm pol}$.

(iii) Finally, the density of the exciton reservoir is adjusted to reproduce the condensate pattern close to the center of the spot.

In Fig. 6(a), the polariton decay rate is taken to $\gamma_{\rm pol} =$ 0.35 meV, i.e. almost half of the photon decay rate $\gamma_{\rm cav}$

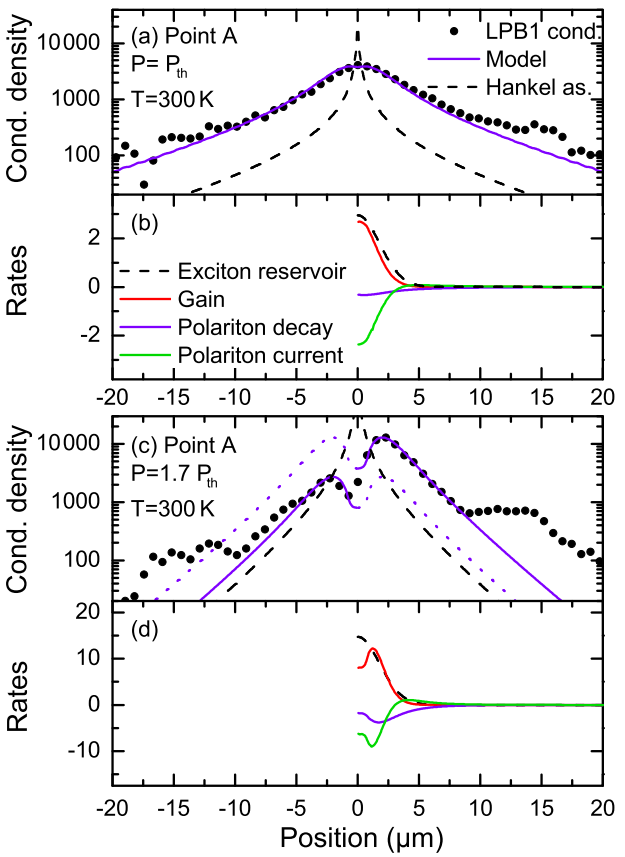

FIG. 6. (Color online) (a) Experimental y-axis profiles of the condensate (dots) at the polariton laser threshold [$P = P_{\rm th}$, LPB1, $T = 300$ K, Fig. 3(f)], GPE simulation (plain line), and asymptotic Hankel function (dashed line). (b) Radial dependence of the simulated rates for gain (stimulated relaxation towards the condensate), polariton decay (losses) and in-plane polariton current. (c) and (d) Same information for $P = 1.7\ P_{\rm th}$. The simulation parameters are summarized in Table III.

obtained from earlier linewidth measurements. This corresponds to a polariton lifetime twice longer than the cavity lifetime. This factor 1/2 is consistent with the 1/2 photonic fraction of the LPB1 polariton branch. When the pumping rate is increased [$P = 1.7\ P_{\rm th}$, Fig. 6(c)], the condensate profile (for distances smaller than 10 μm) decreases more rapidly with r than for $P = P_{\rm th}$, despite a larger wave vector as deduced from the larger blueshift. This can be accounted for with a larger polariton decay rate $\gamma_{\rm pol} = 1.8$ meV due, for example, to the presence of additional decay channels such as scatterings towards other polariton states. This will be discussed in Sec. V.

The determination of the density of the exciton reservoir is more straightforward. The total number of excitons in the reservoir is $N_R = 1.6\ 10^7$ (resp. $4.9\ 10^7$) for $P = P_{\rm th}$ (resp. $P = 1.7\ P_{\rm th}$), corresponding to an exciton density at the center of the spot $n_R(r = 0) = 8\ 10^5\ \mu{\rm m}^{-2}$ (resp. $2.4\ 10^6\ \mu{\rm m}^{-2}$). The increase of n_R by a factor of 3 instead of 1.7 shows that the assumption of a constant relaxation efficiency from the laser energy to the reservoir and/or from the reservoir to the condensate does not fully correspond to the experimental situation.

The formation of a condensate pattern with a local minimum at the laser spot center and local maxima at $r = 2\ \mu$m is a striking feature of the polariton near-field image presented in Figs. 3(e) and 3(f). Even if the experimental pattern is not presenting a cylindrical symmetry as assumed in our model, it is qualitatively reproduced in the simulations. It should be noticed that, for $P = 1.7\ P_{\rm th}$, the pattern profile is very sensitive to the reservoir density, so that any inhomogeneity of the excitation or of the relaxation efficiency induces large variation of the condensate local density due to the nonlinearity of the formation process; such inhomogeneities have a weaker effect for $P \leqslant P_{\rm th}$.

The analysis of the local contributions to the variation of the condensate distribution allows a better understanding of the condensate formation mechanism. As discussed in Ref. [26], the polariton conservation equation in the stationary regime is the sum of three terms (gain, polariton decay, and polariton current):

$$(R\, n_R(\boldsymbol{r}) - \gamma_{\rm pol})|\,\psi(\boldsymbol{r})|^2 - \frac{\hbar}{m^*}\, div(|\,\psi(\boldsymbol{r})|^2 \cdot \boldsymbol{k}(\boldsymbol{r})) = 0, \tag{3}$$

where the local polariton wave vector $\boldsymbol{k}(\boldsymbol{r})$ is obtained as the gradient of the phase of the polariton wave function. At the condensation threshold [$P = P_{\rm th}$, Fig. 6(b)], even if the condensate profile has its maximum at $r = 0$, the polariton current is much larger than the polariton losses, so that the reservoir density $n_R(0) = 8\ 10^5\ \mu{\rm m}^{-2}$ is 16 times larger than $n_{R\ {\rm th}}^{\rm 2D}$ in the 2D case. At $P = 1.7\ P_{\rm th}$, the polariton current and the polariton decay contributions have comparable magnitudes. The polariton condensate radially accelerates and gets amplified on the sides of the exciton reservoir, with a maximum at $r = 2\ \mu$m; at this position, the stimulated relaxation from the exciton reservoir therefore feeds the condensate with polaritons with a nonzero wave vector.

The analysis of the k-space distribution of the condensate is further illustrated in Fig. 7. In order to compare with the experimental cross-section of the far-field pattern of the condensate [Fig. 7(a)], the local polariton wave vector $\boldsymbol{k}(\boldsymbol{r})$ is plotted as a white line in Fig. 7(b), and the emission intensity at the same position is indicated in false colors. Its spatial average provides the simulated far-field pattern of the condensate [Fig. 7(a)]. The simulated and experimental profiles both present a maximum at $k \neq 0$, a signature of the ballistic propagation of the polaritons. However, the wave vector of this maximum is very different: $k = 2\ \mu{\rm m}^{-1}$ for the experiment and $5\ \mu{\rm m}^{-1}$ for the simulation. Much weaker peaks are observed at 4–5 $\mu{\rm m}^{-1}$ in the experimental profile, corresponding to partial rings in the 2D far-field pattern [dashed circles in Fig. 4(c) and 4(e)]. This will be discussed in the Sec. V.

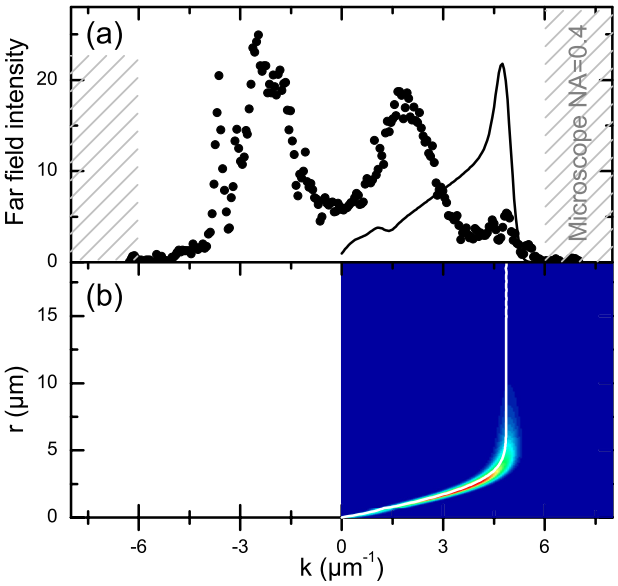

FIG. 7. (Color online) (a) Experimental k_y profiles of the condensate far-field emission (dots) at the polariton laser threshold ($P = 1.7\ P_{\rm th}$, LPB1, $T = 300$ K), and the GPE simulation corresponding to Figs. 6(c) and 6(d) (plain line). (b) Relation between wave vector and radius along the condensate propagation (plain white line). The intensity of the condensate emission is indicated in false colors.

D. Simulations of a polariton condensate at positive detuning

The formation process of the condensate strongly depends on the excitonic character of the polariton branch, i.e. its exciton Hopfield coefficient and more importantly its effective mass, as shown in the following analysis of the experiment performed on LPB2 at $T = 80$ K (Fig. 5). Here, the effective mass of the polariton branch is almost five times larger than the one of the LPB1. The experimental profile of the condensate [$P = 1.3\ P_{\rm th}$, Fig. 8(a)] is dominated by a sharp maximum at $r = 0\ \mu$m, and propagation tails. The measured blueshift is 11 meV, leading to an asymptotic polariton wave vector far from the spot center of 9 $\mu{\rm m}^{-1}$ (beyond the NA of our microscope objective) and an exciton density $n_R(r = 0) = 1.2\ 10^6\ \mu{\rm m}^{-2}$, 20 times larger than the calculated threshold density for an infinite 2D condensate. The parameters of the corresponding simulation are $\gamma_{\rm pol} = 0.35$ meV, as in Fig. 6(a), and $R = 4.9\ 10^{-7}$ meV $\mu{\rm m}^{-2}$ (lower than at $T = 300$ K). Figure 8(b) shows that the condensate is mainly generated at the center of the spot and then propagates outwards without

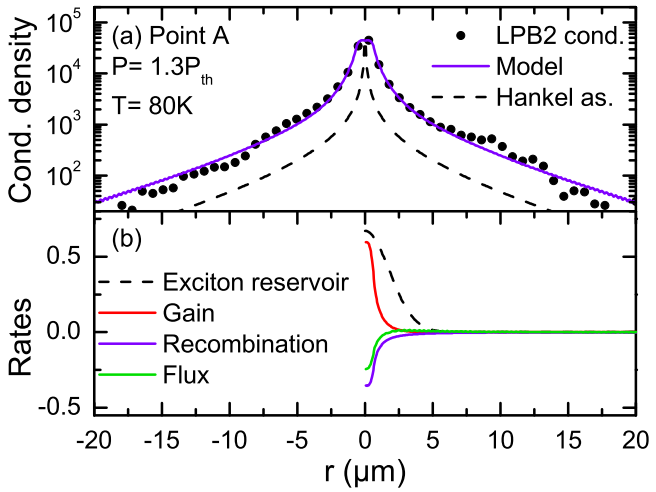

FIG. 8. (Color online) (a) Experimental y-axis profiles of the condensate (dots) above the polariton laser threshold ($P = 1.3\ P_{\rm th}$, LPB2, $T = 80$ K), and GPE simulation (plain line) and asymptotic Hankel function (dashed line); the blueshift of the condensate is 11 meV, as in the corresponding experiment (Fig. 5) and a reservoir density at the center is 7 10^5 cm^{-2}. The polariton decay rate $\gamma_{\rm pol} = 0.4$ meV. (b) Radial dependence of the simulated rates for gain (stimulated relaxation), polariton recombination, and polariton flux.

any amplification, so that the condensate profile is close to the Hankel function.

V. DISCUSSION

The quantitative analysis of the spatial distribution of the polariton condensate in the investigated ZnO microcavity shows that different formation schemes can be involved depending on the detuning of the polariton branch and the excitation density. The most important parameter is the effective mass of the investigated polariton branch. For a given blueshift $\hbar(\omega_c - \omega_0)$, it determines the propagation speed of the polariton wave packet far from the reservoir $v_c = \sqrt{2\,\hbar(\omega_c - \omega_0)/m^*}$, and the order of magnitude of the time spent by the polaritons within the reservoir before free propagation $t_1 = \sigma_R/v_c$ (0.24 ps for LPB1 vs 0.5 ps for LPB2 according to our simulations; σ_R is the waist size of the Gaussian profile of the reservoir). This time t_1 has to be compared to the timescale of the stimulated relaxation from the reservoir to the condensate $t_2 = 1/(R\,n_R)$, which is estimated to be 0.07 ps for LPB1 at 300 K vs 0.8 ps for LPB2 at 80 K. In the case of a "light" polariton branch (LPB1) and an efficient relaxation ($T = 300$ K), the stimulated relaxation is faster than the escape time out of the reservoir, so that the polariton condensate gets amplified as it flows away. This situation presents some analogy with the amplification of a polariton condensate after propagation and reflection, demonstrated in 1D polariton ridges [4]. In the case of a "heavy" polariton branch (LPB2) and a less efficient relaxation ($T = 80$ K), the condensate forms at the center of the reservoir spot and then freely propagates outwards without amplification, like in a "freefall". The difference between those two regimes can be evidenced through the complementary measurements of the real-space and k-space distributions of the polariton condensate. They could not be distinguished in previous studies based only on far-field measurement [16]. Due to the strong correlation between the relaxation efficiency and the detuning of the condensed branch in our multimode ZnO microcavity, two scenarios cannot be explored experimentally in our system, corresponding to an efficient relaxation to a condensate in a heavy LPB, and an inefficient relaxation to a condensate in a light LPB.

The tightly focused excitation regime leads to an increase of the threshold reservoir density for condensation compared to the 2D case of an infinite excitation spot. As discussed in Sec. IV B and illustrated in the two parameter sets in Table III, the estimate of the exciton density at threshold is strongly dependent on the choice of the parameters for interactions (g_R) and stimulated relaxation (R). It also relies on a broad set of experimental results, so that its precise determination is challenging. However, our simulations provide the first estimates of this increase for the investigated case of a nonresonant quasi-cw excitation (400 ps pulses at 4.66 eV, spot diameter 4 μm FWHM). The threshold ratio $n_{R\ \rm th}(0)/n_{R\ \rm th}^{\rm 2D}$ is of the order of 10 to 20 times, with an uncertainty estimated to a factor 2.

The absolute value of the threshold density for condensation cannot be exactly determined. We consider here only one reservoir of excitons, which is involved both in the condensate repulsion (coefficient g_R) and in the stimulated relaxation forming the condensate (coefficient R), leading to a discrepancy with previous theoretical predictions of about one order of magnitude. This may be related to a more complex situation where all photogenerated carriers contribute to the condensate repulsion, whereas only a fraction of them populate the reservoir of excitons and large-k polaritons that can efficiently feed the condensate. Assuming the existence of two distinct reservoirs is a possible way to explain this finding: The exciton reservoir, composed of excitons and large-k polaritons, is involved in the stimulated relaxation term $\hbar R\,n_{R1}$ of the Eq. (2), whereas a second reservoir composed of all the photogenerated carriers (all electron-hole pairs, some of them not yet relaxed to the exciton energy or not able to undergo stimulated relaxation towards the condensate) contribute to the repulsive potential $\hbar g_R\,n_{R2}$ felt by the condensate. This "two reservoirs" assumption is summarized in the Table III and is also debated in the formation of polariton condensates in GaAs and GaN microcavities [33–35].

A second limitation of the present model lies in the absence of relaxation that was recently taken into account in the theoretical modeling of polariton condensation [36]. Indeed, we do not observe energy relaxation of the polaritons within the condensed polariton branch beyond threshold in the recorded spectra, so that the assumption of a negligible energy relaxation is consistent with our experiments. However, a discrepancy is observed between the experimental k-space distribution of the polariton condensate and the simulated one; the polaritons do not reach the predicted maximum value of their wave vector far from the excitation spot. Two possible explanations can be proposed that would also require further investigations: (i) At large polariton densities in the condensate, part of the polaritons are ejected from the condensate towards other polariton branches [18,37], leading

to a decrease of the polariton lifetime; our simulations suggest that even a fourfold increase of the polariton decay rate γ_{pol} is not enough to account for the k-space experimental results. (ii) Even if they do not relax in energy, the polaritons within the condensate may relax their wave vector due to polariton-polariton scattering.

Our model allows one to estimate the populations of the exciton reservoir (absolute particle numbers of the order of 10^7 with our set of parameters) and the condensate (of the order of 10^3), so that we can conclude that (i) there is no depletion of the reservoir and (ii) the polariton-polariton repulsion within the condensate is negligible compared to the one of the reservoir. We should notice that the absence of depletion may be specific to the 400 ps pulsed excitation used in this paper, as well as many previous studies on GaN and ZnO polariton condensation; such pulses are long compared to the typical timescales of the excitons and photons in the system, but they are probably not long enough to reach a stationary regime where the condensate particle number is limited by the depletion of the reservoir.

VI. CONCLUSIONS

We have studied the formation and propagation of a polariton condensate in a ZnO microcavity in the tightly focused excitation regime. The 2D imagery of the spectrally resolved emission in real and reciprocal spaces provides a set of experimental results that can be compared to a simple model based on the GPE. The respective roles of the condensate formation, the repulsion by the exciton reservoir, the condensate amplification, and the condensate propagation are identified. The validity of this model is discussed in depth, as well as the possible sets of physical parameters compatible with the experiments. Two regimes are evidenced depending on the detuning of the condensing polariton branch (through its effective mass) and on the temperature (which plays a central role in enhancing polariton relaxation): Light polaritons near zero exciton-photon detuning propagate slowly enough under the exciton reservoir so that their condensate is strongly amplified "on the fly," whereas heavy polaritons at positive detuning accelerate to larger wave vectors (because of a larger exciton-exciton repulsion) and are not amplified along propagation. Finally, we can estimate the increase of the exciton density at threshold when comparing tightly focused excitation and the ideal case of an infinite 2D system; this factor reaches 10 to 20 in this paper. These considerations are crucial in order to properly design and predict future polariton laser devices based on micron-sized exciton reservoirs.

ACKNOWLEDGMENTS

The authors would like to thank F. Réveret, P. Disseix, J. Leymarie, D. Solnyshkov, and G. Malpuech for fruitful discussions, J. R. Huntzinger for the transfer matrix simulations and H. Gargoubi for her careful reading of the manuscript.

APPENDIX A: MODELING OF THE POLARITON DISPERSION AND THE POLARITON-EXCITON INTERACTION

The multimode character of the investigated microcavity and the very large value of its Rabi splitting requires a detailed modeling of the polariton eigenstates in each lower polariton branch, in order to extract the relevant parameters for the model developed in Sec. IV: the effective masses and the polariton-exciton interaction constants g_R for each branch. Here, g_R is reduced compared to the exciton-exciton interaction constant g_{XX} because the polariton is only partially excitonic in nature. Assuming that the exciton and polariton densities vary on length scales comparable to the optical wavelength, and much larger than the exciton Bohr radius, g_R is obtained by slightly shifting the exciton energy E_X and deducing the corresponding variation of the polariton energy E_{LPB}: It reads $g_R = \frac{\partial E_{\mathrm{LPB}}}{\partial E_X} \cdot g_{XX}$. Indeed, in the presence of an exciton reservoir with a density n_R, the potential energy of an additional exciton reads $\hbar g_{XX}\, n_R$. The potential energy of an additional polariton can be obtained by calculating the corresponding eigenmodes of the exciton-photon system, with an exciton energy shifted by $+\hbar g_{XX}\, n_R$, leading to the blueshift $\hbar g_R\, n_R$ of the polariton branch in the presence of the reservoir.

The usual modeling of the polariton eigenstates is performed through a coupled oscillator model: The exciton-photon interaction is described within a 2×2 matrix, with two main parameters (the exciton-photon detuning and the Rabi splitting). This model allows one to determine the exciton Hopfield coefficient c_X of the polariton wave function and the corresponding exciton content $|c_X|^2$. The polariton effective mass then reads $m^*_{\mathrm{LPB}} = m^*_{\mathrm{cav}}/(1 - |c_X|^2)$, where m^*_{cav} is the effective mass of the bare cavity mode. The interaction constant of a polariton with an exciton is $g_R = |c_X|^2\, g_{XX}$. This model can be extended to the case of multiple cavity modes. In our present microcavity, we can include the three cavity modes cav_0, cav_1, and cav_2, corresponding to the 5λ, 4.5λ, and 4λ resonances of the active layer, leading to a 4×4 matrix.

However, due to the strength of the exciton-photon coupling, the coupled-oscillator approach is not valid for the polariton branches at positive detuning [38]. We therefore prefer to extract directly those parameters from the transfer-matrix simulations, which provide an accurate description of the polariton energy dispersions. Figure 9 presents such a comparison of transfer-matrix simulations and the corresponding coupled oscillator modeling. The agreement of the two approaches is good for most of the polariton branches, but a clear discrepancy is observed when the photon mode cav_1 reaches positive detunings, for angles larger than 25° [38]. Moreover, the LPB2 branch is visible at 3.315 eV in the transfer matrix simulation, whereas it cannot be obtained in the coupled oscillator model. This comparison shows that only the transfer-matrix simulations provide a proper description of the energies of all polariton branches, including at positive detuning, because they take into account the nonperturbative character of the strong exciton-photon interaction in ZnO microcavities. The same simulations also provide the dependence of the polariton branches as a function of the cavity thickness, as shown in Fig. 1 of Ref. [20].

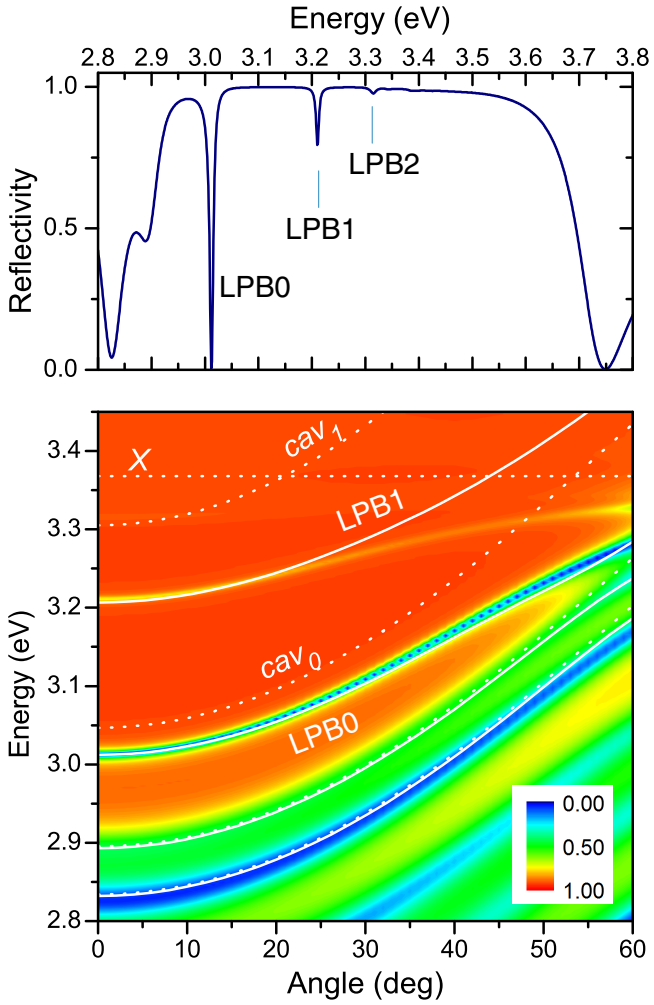

FIG. 9. (Color online) (a) Transfer-matrix simulation of the reflectivity of the microcavity at normal incidence (transverse magnetic polarization) for a cavity thickness $L = 890$ nm, and a temperature $T = 80$ K. (b) Angular dependence of the reflectivity (false colors). The bare exciton and photon modes and the dispersion of the polariton branches deduced from the coupled oscillator model are indicated as dashed and plain lines respectively. The parameters are summarized in Table I.

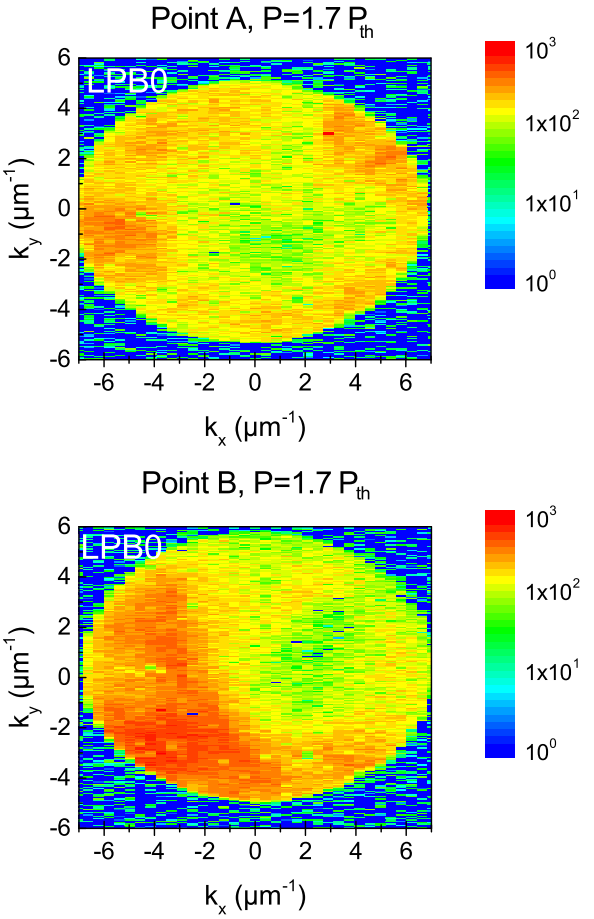

FIG. 10. (Color online) Far-field images of the uncondensed LPB0 polaritons at points A and B, above threshold ($T = 300$ K, logarithmic color scales).

The variation of the energies of the polariton branches has been calculated for small variations of the exciton energy $x = \frac{\partial E_{\mathrm{LPB}}}{\partial E_X}$ or the cavity thickness $\frac{\partial E_{\mathrm{LPB}}}{\partial L}$. The polariton-exciton interaction constant is then taken as $g_R = x\, g_{XX}$. The results are presented in the Table I, together with the detunings, effective masses, and Rabi splittings of the investigated polariton branches. The Rabi splitting of the investigated 4.5λ cavity mode is slightly larger than the one measured for a 2.5λ cavity mode in Ref. [20]. The estimate of the parameter x is comparable to the exciton content $|c_X|^2$ at negative detuning and becomes larger at zero and positive detunings. This result may be counterintuitive since the sum of the coefficients x for all branches is larger than unity, contrary to the sum of their $|c_X|^2$ Hopfield coefficients deduced from the diagonalization of the coupled oscillator Hamiltonian. This is due to the multimode character of the microcavity and to the large sensitivity of the most excitonic polariton branches on the bare exciton energy.

APPENDIX B: PROPAGATION OF THE POLARITONS IN THE UNCONDENSED BRANCH LPB0

The impact of the cavity thickness gradient on the propagation of the polaritons is evidenced in the near-field emission patterns shown in Fig. 3. The gradient at point B induces a 3 μm shift of the uncondensed polaritons in the photonic LPB0 branch. This translation of the LPB0 polaritons can also be seen in the far-field patterns, as shown on the Fig. 10. At point A, the k-space distribution of the LPB0 polaritons is rather isotropic, with a large amount of emission near and beyond 4–6 $\mu\mathrm{m}^{-1}$, i.e. the accessible NA of our microscope objective; this reflects their out-of-equilibrium distribution and the so-called relaxation bottleneck. At point B, the distribution is not isotropic, with a stronger emission in one half of the observable k-space that points in the direction of the photonic gradient seen in Fig. 1(b); this reflects the drift of the uncondensed polaritons along the photonic gradient.

[1] B. Nelsen, G. Liu, M. Steger, D. W. Snoke, R. Balili, K. West, and L. Pfeiffer, Phys. Rev. X **3**, 041015 (2013).

[2] B. Sermage, G. Malpuech, A. V. Kavokin, and V. Thierry-Mieg, Phys. Rev. B **64**, 081303 (2001).

[3] M. Steger, G. Liu, B. Nelsen, C. Gautham, D. W. Snoke, R. Balili, L. Pfeiffer, and K. West, Phys. Rev. B **88**, 235314 (2013).

[4] E. Wertz, A. Amo, D. D. Solnyshkov, L. Ferrier, T. C. H. Liew, D. Sanvitto, P. Senellart, I. Sagnes, A. Lemaître, A. V. Kavokin, G. Malpuech, and J. Bloch, Phys. Rev. Lett. **109**, 216404 (2012).

[5] T. Gao, P. S. Eldridge, T. C. H. Liew, S. I. Tsintzos, G. Stavrinidis, G. Deligeorgis, Z. Hatzopoulos, and P. G. Savvidis, Phys. Rev. B **85**, 235102 (2012).

[6] H. S. Nguyen, D. Vishnevsky, C. Sturm, D. Tanese, D. Solnyshkov, E. Galopin, A. Lemaître, I. Sagnes, A. Amo, G. Malpuech, and J. Bloch, Phys. Rev. Lett. **110**, 236601 (2013).

[7] D. D. Solnyshkov, H. Terças, and G. Malpuech, Appl. Phys. Lett. **105**, 231102 (2014).

[8] K. G. Lagoudakis, M. Wouters, M. Richard, A. Baas, I. Carusotto, R. André, L. S. Dang, and B. Deveaud-Plédran, Nat. Phys. **4**, 706 (2008).

[9] D. Sanvitto, F. M. Marchetti, M. H. Szymanska, G. Tosi, M. Baudisch, F. P. Laussy, D. N. Krizhanovskii, M. S. Skolnick, L. Marrucci, A. Lemaitre, J. Bloch, C. Tejedor, and L. Vina, Nat. Phys. **6**, 527 (2010).

[10] A. Amo, S. Pigeon, D. Sanvitto, V. G. Sala, R. Hivet, I. Carusotto, F. Pisanello, G. Leménager, R. Houdré, E. Giacobino, C. Ciuti, and A. Bramati, Science **332**, 1167 (2011).

[11] R. Hivet, H. Flayac, D. D. Solnyshkov, D. Tanese, T. Boulier, D. Andreoli, E. Giacobino, J. Bloch, A. Bramati, G. Malpuech, and A. Amo, Nat. Phys. **8**, 724 (2012).

[12] M. Sich, D. N. Krizhanovskii, M. S. Skolnick, A. V. Gorbach, R. Hartley, D. V. Skryabin, E. A. Cerda-Méndez, K. Biermann, R. Hey, and P. V. Santos, Nat. Photon **6**, 50 (2012).

[13] P. M. Walker, L. Tinkler, D. V. Skryabin, A. Yulin, B. Royall, I. Farrer, D. A. Ritchie, M. S. Skolnick, and D. N. Krizhanovskii, Nat. Commun. **6**, 8317 (2015).

[14] I. Carusotto and C. Ciuti, Rev. Mod. Phys. **85**, 299 (2013).

[15] T. Guillet, M. Mexis, J. Levrat, G. Rossbach, C. Brimont, T. Bretagnon, B. Gil, R. Butté, N. Grandjean, L. Orosz, F. Reveret, J. Leymarie, J. Zúñiga-Pérez, M. Leroux, F. Semond, and S. Bouchoule, Appl. Phys. Lett. **99**, 161104 (2011).

[16] H. Franke, C. Sturm, R. Schmidt-Grund, Gerald Wagner, and M. Grundmann, New J. Phys. **14**, 013037 (2012).

[17] L. Orosz, F. Réveret, F. Médard, P. Disseix, J. Leymarie, M. Mihailovic, D. Solnyshkov, G. Malpuech, J. Zúñiga-Pérez, F. Semond, M. Leroux, S. Bouchoule, X. Lafosse, M. Mexis, C. Brimont, and T. Guillet, Phys. Rev. B **85**, 121201 (2012).

[18] W. Xie, H. Dong, S. Zhang, L. Sun, W. Zhou, Y. Ling, J. Lu, X. Shen, and Z. Chen, Phys. Rev. Lett. **108**, 166401 (2012).

[19] T.-C. Lu, Y.-Y. Lai, Y.-P. Lan, S.-W. Huang, J.-R. Chen, Y.-C. Wu, W.-F. Hsieh, and H. Deng, Opt. Express **20**, 5530 (2012).

[20] F. Li, L. Orosz, O. Kamoun, S. Bouchoule, C. Brimont, P. Disseix, T. Guillet, X. Lafosse, M. Leroux, J. Leymarie, M. Mexis, M. Mihailovic, G. Patriarche, F. Réveret, D. Solnyshkov, J. Zúñiga-Pérez, and G. Malpuech, Phys. Rev. Lett. **110**, 196406 (2013).

[21] A. Trichet, E. Durupt, F. Médard, S. Datta, A. Minguzzi, and M. Richard, Phys. Rev. B **88**, 121407 (2013).

[22] D. Xu, W. Xie, W. Liu, J. Wang, L. Zhang, Y. Wang, S. Zhang, L. Sun, X. Shen, and Z. Chen, Appl. Phys. Lett. **104**, 082101 (2014).

[23] J. Wang, W. Xie, L. Zhang, Y. Wang, J. Gu, T. Hu, L. Wu, and Z. Chen, Solid State Commun. **211**, 16 (2015).

[24] K. S. Daskalakis, S. A. Maier, and S. Kéna-Cohen, Phys. Rev. Lett. **115**, 035301 (2015).

[25] M. Wouters and I. Carusotto, Phys. Rev. Lett. **99**, 140402 (2007).

[26] M. Wouters, I. Carusotto, and C. Ciuti, Phys. Rev. B **77**, 115340 (2008).

[27] F. Li, L. Orosz, O. Kamoun, S. Bouchoule, C. Brimont, P. Disseix, T. Guillet, X. Lafosse, M. Leroux, J. Leymarie, G. Malpuech, M. Mexis, M. Mihailovic, G. Patriarche, F. Reveret, D. Solnyshkov, and J. Zuniga-Perez, Appl. Phys. Lett. **102**, 191118 (2013).

[28] C. Brimont, T. Guillet, S. Rousset, D. Néel, X. Checoury, S. David, P. Boucaud, D. Sam-Giao, B. Gayral, M. J. Rashid, and F. Semond, Opt. Lett. **38**, 5059 (2013).

[29] M. Aßmann, F. Veit, M. Bayer, A. Löffler, S. Höfling, M. Kamp, and A. Forchel, Phys. Rev. B **85**, 155320 (2012).

[30] M. Thunert, A. Janot, H. Franke, C. Sturm, T. Michalsky, M. D. Martin, L. Viña, B. Rosenow, M. Grundmann, and R. Schmidt-Grund, arxiv:1412.8667 (2014).

[31] H. Haug and S. Koch, Phys. Status Solidi B **82**, 531 (1977).

[32] A. Kavokin, J. Baumberg, G. Malpuech, and F. Laussy, *Microcavities* (Oxford Science Publications, Oxford, 2006).

[33] G. Nardin, K. G. Lagoudakis, M. Wouters, M. Richard, A. Baas, R. André, L. S. Dang, B. Pietka, and B. Deveaud-Plédran, Phys. Rev. Lett. **103**, 256402 (2009).

[34] I. Iorsh, M. Glauser, G. Rossbach, J. Levrat, M. Cobet, R. Butté, N. Grandjean, M. A. Kaliteevski, R. A. Abram, and A. V. Kavokin, Phys. Rev. B **86**, 125308 (2012).

[35] M. Amthor, T. C. H. Liew, C. Metzger, S. Brodbeck, L. Worschech, M. Kamp, I. A. Shelykh, A. V. Kavokin, C. Schneider, and S. Höfling, Phys. Rev. B **91**, 081404 (2015).

[36] D. D. Solnyshkov, H. Terças, K. Dini, and G. Malpuech, Phys. Rev. A **89**, 033626 (2014).

[37] C. P. Dietrich, R. Johne, T. Michalsky, C. Sturm, P. Eastham, H. Franke, M. Lange, M. Grundmann, and R. Schmidt-Grund, Phys. Rev. B **91**, 041202 (2015).

[38] T. Guillet, C. Brimont, P. Valvin, B. Gil, T. Bretagnon, F. Médard, M. Mihailovic, J. Zúñiga-Pérez, M. Leroux, F. Semond, and S. Bouchoule, Phys. Status Solidi C **9**, 1225 (2012).